1 My name is Jeffrey Uncu (jeffrey.uncu@mail.utoronto.ca, University of Toronto), I am

2 from Professor Nicolas Grisouard's (nicolas.grisouard@utoronto.ca, University of Toronto)

3 group at the University of Toronto. My co-author and I are pleased to submit this manuscript

4 titled "Wave Scattering by an Isolated Cyclogeostrophic Vortex". This paper is a non-peer

5 reviewed preprint submitted to EarthArXiv. We have submitted to the Journal of Fluid

6 Mechanics (JFM) for peer review on February 21, 2024, and then received major revisions

7 on April 5th, 2024. This version represents the version which was resubmitted to JFM on

8 August 2nd 2024.

Wave Scattering by an Isolated Cyclogeostrophic Vortex

Jeffrey Uncu† **and Nicolas Grisouard**

Department of Physics, University of Toronto, Toronto, ON M5S 1A7, Canada

The propagation paths of oceanic internal tides are influenced by their interactions with vortices. We examine the scattering effect that an isolated vortex in (cyclo)geostrophic balance has on a rotating shallow-water plane wave. We run a suite of simulations in which we vary the non-dimensional vorticity of the vortex, Ro, the relative scale of the vortex size to the Rossby radius of deformation, Bu, and the size of the vortex compared to the plane wave wavelength, K. We compare the scattered wave flux pattern to ray-tracing predictions. Ray tracing predictions are relatively insensitive to K in the $1 < K < 4$ range we investigate; however, they generally underestimate the broad angles of the shallow-water wave scattering patterns, especially for the lower end of the K range. We then measure the ratio of the scattered wave energy flux to the incoming wave energy flux, denoted as S for each simulation. We find that S follows a power law $S \propto (FrK)^2$ when $S < 0.2$, where $Fr = Ro/\sqrt{Bu}$ is the Froude number. When $S > 0.2$, it starts plateauing.

† Email address for correspondence: jeffrey.uncu@mail.utoronto.ca

Abstract must not spill onto p.2

1. Introduction

When the barotropic tide oscillates over the bathymetry of the ocean, it creates internal tides (ITs). These are internal waves that oscillate at or near the generating tidal frequencies (Garrett & Kunze 2007). Of the 4 TW that are injected into the ocean by astronomical forcing, approximately 2.4 TW are transferred to ITs (Egbert & Ray 2003). Most of their energy is lost to turbulent mixing at the generation sites, while about 10-40% propagate away (Egbert & Ray 2000). Low modes can propagate thousands of kilometres, making the details of their horizontal propagation critical to determining where they will eventually dissipate (Zhao *et al.* 2016). This makes them an essential aspect for forecasting climate and tuning general circulation models (de Lavergne *et al.* 2019).

Unlike the barotropic tide, which oscillates in phase with astronomical forcing, IT features are more susceptible to evolve as a result of changing ocean conditions throughout its propagation (Nash *et al.* 2012). These changes include evolving local stratification, and, of note for this study, eddies. At mid-latitudes, mesoscale eddies ($\sim$ 100 km wide) are well described by quasi-geostrophic models. These are flows with negligible advective effects, and whose dynamic evolution is dominantly characterised by a balance between Coriolis and pressure forces, which leads us to hereafter refer to these flows as 'balanced'. They feature small Rossby numbers $Ro = U/(Lf)$, where U and L are characteristic eddy velocity and length scales, respectively, and f is the local Coriolis parameter.

Advances in satellite altimetry in the 1990s, starting with the TOPEX/Poseidon mission, provided the first global visualisations of large-scale currents and of the mesoscale eddy field (Fu *et al.* 1994). This allowed Rainville & Pinkel (2006) to calculate the propagation paths of mode-1 to mode-5 ITs using ray-tracing. They also show that higher modes are more susceptible to phase shifts by the balanced flow, causing an apparent loss in IT energy when measured by harmonically filtering narrow bands around the tidal frequencies. However, ray

tracing assumes that the IT horizontal wavelength λ is small compared to the length scale of variations in the eddy velocity L. Mesoscale eddies usually have length scales smaller than the largest mode-1 semi-diurnal tides at mid-latitudes, but are typically larger than higher IT modes. As such, ray tracing is effective only for higher modes in principle, but is often used when length scales are similar. Chavanne *et al.* (2010) used 3D ray tracing to model wave propagation of an IT with a 50 km wavelength through a 55 km vortex inspired by a vortex near the Hawaiian ridge. They showed that even near generation sites, the IT can become very incoherent, that is, it can develop significant and time-evolving phase shifts with the astronomical forcing. They also showed that IT energy could be amplified up to a factor of 15 in the core of the vortex.

New remote sensing satellites, such as the Surface Water and Ocean Topography (SWOT) mission (Morrow *et al.* 2019) resolve scales up to a few tens of kilometres. The increased resolution should enable us to observe higher Rossby numbers and shorter IT wavelengths, prompting researchers to use new techniques to further refine the mapping of ITs that do not use the ray tracing assumption. One such technique is the kinetic equation developed in Savva & Vanneste (2018), Kafiabad *et al.* (2019) and Savva *et al.* (2021) that models the redistribution of inertia-gravity wave energy in position-wavenumber phase space when embedded in quasi-geostrophic turbulence. This method, however, requires a small Rossby number. A powerful deterministic method that does not assume length scale separation is triad resonance theory. Ward & Dewar (2010) used triad resonance theory to describe the evolution of a wave mode embedded in a balanced flow in the one-layer rotating shallow-water equations (RSWEs). In this interaction, the balanced flow provides a pathway for the waves to exchange energy with other waves of constant frequency. This method clearly illustrates how the advection term couples the balanced mode and wave mode to force the linear equations of motion at resonant wave modes. This so-called 'catalytic interaction' of

Focus on Fluids articles must not exceed this page length

a potential vorticity mode (i.e., a mode whose features can theoretically be entirely derived from potential vorticity inversion) and two wave modes was first described in Lelong & Riley (1991) and later in Bartello (1995). However, as the Rossby number increases and the duration of the scattering process increases, near-resonant triads and higher-order non-linearities become increasingly significant, and thus, a solution that only considers resonant triads becomes increasingly inaccurate.

In this article, we model the interaction between an isolated balanced cyclogeostrophic vortex and a Poincaré wave by numerically solving the single-layer RSWEs. Indeed, in isolation, any internal tide mode of a stratified, rotating fluid obeys a set of RSWEs, with the parameters appropriately redefined (e.g., Vallis 2017, § 3.4). This allows us to explore the parameter space spanned by Rossby numbers that range from very small to $O(1)$ values, vortex scales that widely straddle the Rossby radius of deformation, and Poincaré wavelengths that are four times smaller than the vortex scale to as large as the vortex. We first qualitatively compare the scattered wave flux to ray-tracing predictions. We then calculate the amount of energy that is transferred from the incoming wave to the scattered waves for each simulation and then find the scaling relations given the wave and vortex parameters. These interactions are expected to be ubiquitous in the ocean, with applications for diagnosing processes in global circulation models and satellite altimetry data.

2. Methods

2.1. *Physical and mathematical setup*

Here, we describe our equations and the processes we model, which we summarise in figure 1.

We solve the RSWEs on a square domain of side length L_x, with which we associate a Cartesian coordinate system (x, y) centred in the middle of the domain. The layer is under gravitational acceleration g, has depth at rest H, and rotates as an f-plane. These parameters
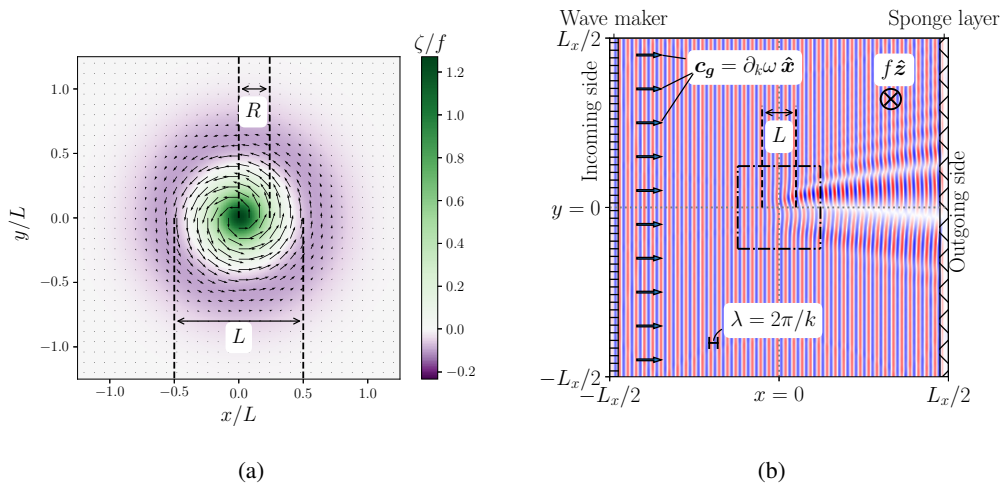
(a)   (b)

Figure 1: Setup for the simulation with parameters $Ro_\zeta = -1.27$, $Bu = 1.76$, $K = 3.0$. (a)

Normalised vorticity field for an isolated anticyclonic cyclogeostrophic vortex. Black

arrows represent the vortex velocity vectors. (b) Height field for a Poincaré wave that is

forced from the left side of the domain and interacts with the isolated vortex pictured in

(a). The black dash-dotted square in (b) aligns with the bounds of panel (a).

define a non-rotating speed $c_0 = \sqrt{gH}$ and a Rossby radius of deformation $L_d = c_0/f$. The

forced-dissipated one-layer RSWEs are

$$\partial_t \boldsymbol{u} + \boldsymbol{u} \cdot \boldsymbol{\nabla} \boldsymbol{u} + g\boldsymbol{\nabla} h + f\hat{\boldsymbol{z}} \times \boldsymbol{u} - \mu\boldsymbol{\nabla}^4 \boldsymbol{u} = \boldsymbol{F}_w(x,t) + \boldsymbol{S}_w(x) \quad \text{and} \qquad (2.1a)$$

$$\partial_t h + h\boldsymbol{\nabla} \cdot \boldsymbol{u} + \boldsymbol{u} \cdot \boldsymbol{\nabla} h - \mu\boldsymbol{\nabla}^4 h = F_h(x,t) + S_h(x), \qquad (2.1b)$$

97   where $\boldsymbol{u} = (u, v)$ is the horizontal velocity field, $\boldsymbol{\nabla} = (\partial_x, \partial_y)$ is the horizontal del operator,

98   μ is the kinematic hyperviscosity (utilised only to provide numerical stability), and h is the

99   height of the total water column. The terms $\boldsymbol{F}_w$, $\boldsymbol{S}_w$, F_h and S_h on the right-hand sides are

100   wave forcing and sponge layer terms, which we describe in more detail later.

101   Our initial condition consists of an axisymmetric circular vortex centred at the origin of

102   the domain. We achieve this through a three-step process. (i) First, we create a Gaussian

103 vortex in geostrophic balance following

$$\left[u_\Theta^{(0)}, \, h_\Theta^{(0)} \right] = \left[\pi^2 fr, \, \frac{H}{Bu_0} \right] Ro \exp\left(-\frac{r^2}{2(L/\pi)^2} \right), \qquad (2.2)$$

105 where $u_\Theta^{(0)}$ and $h_\Theta^{(0)}$ are the initial tangential velocity and height fields of this vortex,

106 L its characteristic width, $Bu_0 = (L_d/L)^2$ is the Burger number, and r is the distance

107 from the centre of the vortex. While Eq. (2.2) is a relatively good approximation for a

108 quasi-geostrophic vortex, water parcels in a vortex with higher Ro experience a significant

109 centrifugal acceleration, which modifies the balance. Applying the iterative method of Penven

110 *et al.* (2014), which we detail in Appendix A, to Eq. (2.2) yields velocity fields $u_\Theta^{(1)}$ and $h_\Theta^{(1)}$

111 that are one step closer to achieving cyclogeostrophic balance. We then use these velocity

112 and height fields as initial conditions for an unforced RSWE simulation. After a transitory

113 adjustment in the form of waves radiating from the vortex and being dissipated by additional

114 sponge layers (see Appendix B), and a rearrangement of the water parcels, a stationary vortex

115 remains. Finally, we save the velocity and height fields $u_\Theta^{(2)}$ and $h_\Theta^{(2)}$ to be used later as initial

116 conditions for our forced simulations. We repeat this procedure for as many initial vortices

117 as we need. For all simulations, $L = 25$ km and $f = -10^{-4}$ s^{-1}. Note that at the end of this

118 procedure, the vortex has departed from the purely Gaussian shape of Eq. (2.2), especially

119 for high Rossby and Burger numbers, for which the adjustment is the strongest.

120 The adjusted vortex length is defined as $L_a = \pi R$, where R is the radius of the maximum

121 tangential velocity $U_q = u_\Theta^{(2)}(R)$, as shown in figure 1a. We define its vorticity Rossby

122 number and bulk Rossby number as

$$Ro_\zeta = \frac{\zeta}{f}\bigg|_{x=y=0} \quad \text{and} \quad Ro_b = \frac{U_q}{L_a f}, \qquad (2.3)$$

124 respectively, where $\zeta = \partial_x v - \partial_y u$ is the vertical vorticity (note that at this point, no other

125 form of motion is present in the domain).

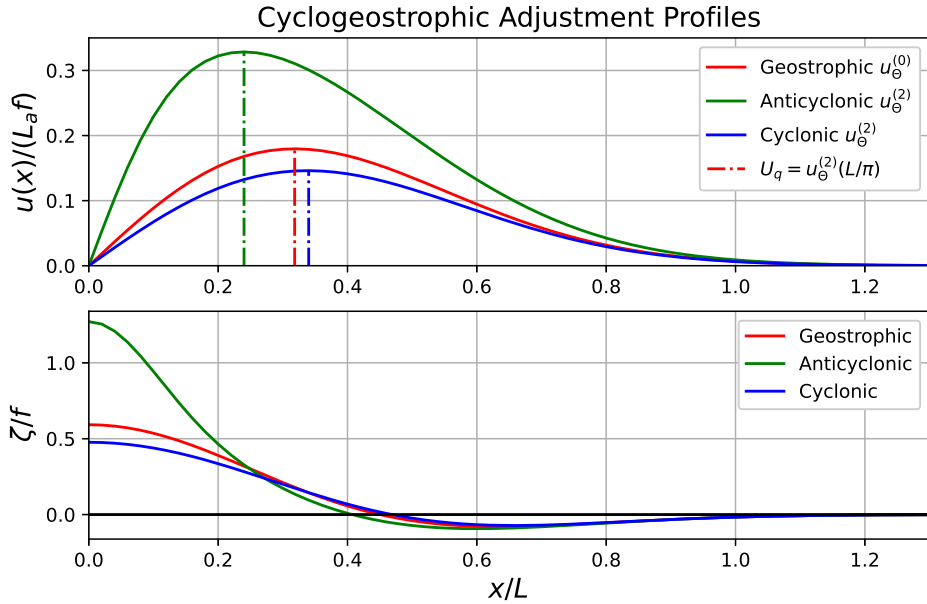126 The resultant azimuthal velocity and vorticity profiles are shown in figure 2. For a

Figure 2: Azimuthal velocity profiles of a pair of cyclonic (solid blue) and anticyclonic

(solid green) vortices that originally started from the same geostrophically-balanced

velocity profile (solid red) with bulk Rossby number $Ro_b = 0.18$. The final normalised

velocity profiles are shown in the upper figure, and the normalised vorticity profiles are

shown in the lower figure. The vertical dashed-dotted lines correspond to the position

$x = R$, where velocity is maximum. The anticyclonic profiles are flipped over the x-axis to

easily compare with the cyclonic profiles.

given value of Ro_b, cyclogeostrophic balance makes the cyclonic vortices wider than their

geostrophic counterparts. For a cyclonic vortex in the southern hemisphere, the inward

pressure gradient must balance not only the outward Coriolis force, but also the centrifugal

force. Thus, a decrease in velocities near the initialised geostrophic value of U_q is needed to

achieve balance, leading to a wider shape. On the other hand, for anticyclonic vortices, the

centrifugal force and pressure gradient are outward and balance the inward Coriolis force.

Thus, the velocity increases, leading to a narrower profile (Shakespeare 2016).

In order to capture this cyclonic/anticyclonic asymmetry in the cyclogeostrophic vorticity

135 distributions, which the bulk Rossby number misses, we also measure the enstrophy, ε, of

136 each vortex, defined below as the integral of the square of the vorticity,

$$\varepsilon' = \iint \zeta^2 \, \mathrm{d}x \, \mathrm{d}y. \qquad (2.4)$$

138 Enstrophy is a convenient method for measuring the strength of the vortex for two reasons.

139 First, the vorticity is the most relevant quantity for scattering. This is expected from ray-

140 tracing theory, which predicts that at leading order in vortex velocity U, the vortical part

141 of the mean flow will rotate the wave vector $\boldsymbol{k}$, while the divergent part will only affect

142 the ray paths at a higher order (Bühler 2014, §4.4.3). This rotation of the wave vector is

143 the main form of scattering that we expect in our experiments. This is consistent with triad

144 resonance theory, which dictates that the dominant triad interaction between the vortex and

145 the wave flow produces a discrete rotation of the wave vector. Second, enstrophy integrates

146 the vorticity over the whole domain and therefore captures some of the information about

147 the spatial structure of the anticyclonic and cyclonic profiles created after cyclogeostrophic

148 adjustment. We non-dimensionalise enstrophy with $\varepsilon = \varepsilon'/(L_a^2 f^2)$.

149 We then generate a plane wave on the boundary at $x = -L_x/2$, hereafter referred to as the

150 "incoming side". It propagates along x with wavenumber $\boldsymbol{k}_i = (2\pi\lambda^{-1}, 0)$, where λ is the

151 wavelength, and frequency $\omega_0 = \sqrt{f^2 + c_0^2 k_i^2}$ with corresponding period $P = 2\pi\omega_0^{-1}$. We

152 generate this wave via the forcing terms

$$\boldsymbol{F}_w = \tau_w^{-1} \left(\boldsymbol{U}_w - \boldsymbol{u} \right) \Pi_w \quad \text{and} \quad F_h = \tau_w^{-1} \left(H_w - h \right) \Pi_w, \qquad (2.5)$$

154 which first appeared in Eqs. (2.1), where $\tau_w = P$ is the wave restoration time scale. In these

155 forcing terms, the fields $(\boldsymbol{u}, h)$ are restored to values $(\boldsymbol{U}_w, H_w)$ that satisfy the polarisation

156 relations for Poincaré waves (see Appendix C), that is,

$$\boldsymbol{U}_w = Fr_w c_0 \left(1, \frac{\omega_0}{f} \right) \cos(|\boldsymbol{k}_i|x - \omega_0 t) \quad \text{and} \quad H_w = \frac{|\boldsymbol{k}_i|H}{f} \sin(|\boldsymbol{k}_i|x - \omega_0 t), \qquad (2.6)$$

158 where $Fr_w = U_w/c_0$ is the wave Froude number, which we keep small throughout this article

to keep the waves linear. This forcing occurs over a limited spatial window along x, following

$$\Pi_w = \Pi\left(x, -L_x/2\right), \tag{2.7}$$

where $\Pi(x, x_0)$ is a Tukey window that we detail in Appendix B.

At the boundary $x = +L_x/2$, hereafter referred to as the "outgoing side", a sponge layer absorbs waves through the sponge terms

$$\boldsymbol{S}_w = -\tau_s^{-1}\boldsymbol{u}\Pi_s \quad \text{and} \quad S_h = \tau_s^{-1}(H - h)\Pi_s, \quad \text{where} \quad \Pi_s = \Pi[x, L_x/2 - \lambda], \tag{2.8}$$

and $\tau_s = 0.05P$ is the sponge restoration time scale. We verified that the vortex remains unaffected by the wave: for our purposes, it does not move, deform, lose, or gain energy in any detectable manner. The result is a time-independent scattering amplitude pattern induced by the vortex shown in figure 1b.

2.2. *Numerical setup and experimental design*

We use Dedalus (Burns *et al.* 2020) to solve the RSWEs spectrally with periodic boundaries in the horizontal directions. We use 512 points in each direction with a uniform spacing of $dx = L/50$. The time step is determined by the vortex strength using the Courant-Friedrichs-Lewy condition $dt < 10^{-2}dx/|U_q|$. The simulation time for each experiment is $t_s = 4t_T/3$, where $t_T = L_x k/\omega_0$ is the transit time of the wave phase across the domain. In practice, the phase and group speeds of the incoming waves are similar in magnitude, and thus t_T is sufficient time for the wave packets to reach the other side of the domain.

To initialise the simulations, we define the unadjusted ratio of the vortex length scale to the wavelength of the incoming wavelength $K_0 = L/\lambda$, which we vary in the range $1 \leqslant K_0 \leqslant 4$. In doing so, we test the consequences of violating the traditional ray-tracing assumption, which requires $K_0 \gg 1$. Similarly, we initialise the unadjusted Burger number as $Bu_0 = (L_d/L)^2$ from 0.5 to 1.5. McWilliams (2016) noted that the size of realistic vortices is around the radius of deformation L_d. However, we find that they are stable at various scales and explore multiple

Rapids articles must not exceed this page length

Parameter	Anticylonic	Cyclonic
Ro_ζ	$-1.27, -0.54, -0.22, -0.13$	$0.18, 0.47, 0.60, 0.89$
Ro_b ($\times 100$)	$-10.46, -5.07, -2.16, -1.19$	$1.80, 4.65, 5.98, 7.96$
ε ($\times 100$)	$19.02, 4.39, 0.80, 0.24$	$0.55, 3.71, 6.12, 11.01$
$Bu(L_a/L)^2 = Bu_0$	$0.5, 0.9, 1.0, 1.1, 1.5$	$0.5, 0.9, 1.0, 1.1, 1.5$
$K(L_a/L)^{-1} = K_0$	$1, 1.5, 2, 3, 4$	$1, 1.5, 2, 3, 4$

Table 1: Simulation parameters shown as initialisation before adjustments are made.

regimes for completeness. Due to the different adjustment processes between cyclonic and anticyclonic vortices, for a given initial L, the adjusted length scale ratio $K = L_a/\lambda$ is not the same for the cyclonic and anticyclonic simulations. In the end, K ranges from 0.5 to 4.5, and similarly, the adjusted Burger numbers $Bu = (L_d/L_a)^2$ range between 0.43 to 2.6. We use vortices whose values for Ro_ζ vary from -1.27 to 0.89. We keep $Fr_w < 10^{-3}$ for all simulations to avoid non-linear steepening and wave-wave interactions between the different components of the incoming and scattered waves. Our suite of simulations consists of all combinations of the Rossby numbers, Burger numbers, and length scale ratios shown in table 1, resulting in a total of 200 simulations.

2.3. *Diagnostics*

In this section, we show how to extract the scattered wave fields from the simulation outputs. We then demonstrate how to calculate the phase-averaged flux and outline the process for calculating the ratio of wave energy scattered by the vortex.

Because the vortex does not evolve during the course of our simulations, we extract the wave field $(\boldsymbol{u}_w, h_w)$ simply by subtracting the initial conditions from the simulation output, that is, $\boldsymbol{u}_w = \boldsymbol{u} - \boldsymbol{u}_\Theta^{(2)}$ and $h_w = h - h_\Theta^{(2)}$. After the wave has reached the sponge layer, the

199 sub-domain defined by a square of length $4L$ centred at the origin will have a wave field

200 pattern that is constant in time if averaged over one period P. We define the phase-averaged

201 energy flux density with

$$\boldsymbol{\phi}_X = \frac{1}{2}c_0^2 \boldsymbol{u}_X \eta_X \quad \text{and} \quad \overline{\boldsymbol{\phi}}_X = \frac{1}{P}\left|\int_{t_p}^{t_p+P} \boldsymbol{\phi}_X \,\mathrm{d}t\right|, \tag{2.9}$$

203 where $\eta_X = h_X - H$ and $t_p > 0.9 t_T$, which ensures the wave has propagated past the vortex

204 but has not yet wrapped around the periodic boundaries. The subscript X denotes which field

205 is used. For example, $X = w$ denotes the phase-averaged total wave flux $\overline{\boldsymbol{\phi}}_w$, which we show

206 in figure 3a for a typical total wave field.

207 To isolate only the flux of the scattered waves $\overline{\boldsymbol{\phi}}_s$ shown in figure 3b, we take a 2D Fourier

208 transform of u_w, v_w, and h_w and cancel the amplitudes of the Fourier modes whose wave

209 vectors are parallel to the incoming wave vector $\boldsymbol{k}_i$. We then take an inverse Fourier transform

210 to obtain u_s, v_s, and h_s, which we use to calculate $\overline{\boldsymbol{\phi}}_s$ using equation (2.9).

211 To calculate the ratio of scattered wave flux to incoming wave flux, we define the control

212 volume shown in figure 3, which is made up of four boundaries located away from the vortex.

213 The incoming boundary is placed at $x/L = -2$, spans $-2 \leqslant y/L \leqslant 2$, and has unit normal

214 vector $\boldsymbol{n}_{in} = (-1, 0)$. Given that we observe the backscatter to be negligible, all of the energy

215 enters through this boundary. We define the outgoing boundary as a semicircle in the $x > 0$

216 half-plane, centred around the origin, of radius $x/L = 2$, where virtually all of the energy

217 exits. We denote $\boldsymbol{n}_{out}$ as the unit vector normal to this boundary. There is virtually no energy

218 moving through the top and bottom boundaries shown in dashed blue lines.

219 The total incoming and scattered fluxes are then

$$\Phi_{in} = \int \overline{\boldsymbol{\phi}}_w \cdot \boldsymbol{n}_{in} \,\mathrm{d}s \qquad \text{and} \qquad \Phi_s = \int \overline{\boldsymbol{\phi}}_s \cdot \boldsymbol{n}_{out} \,\mathrm{d}s, \tag{2.10}$$

221 integrated along the incoming and outgoing boundaries, respectively. To compare how much
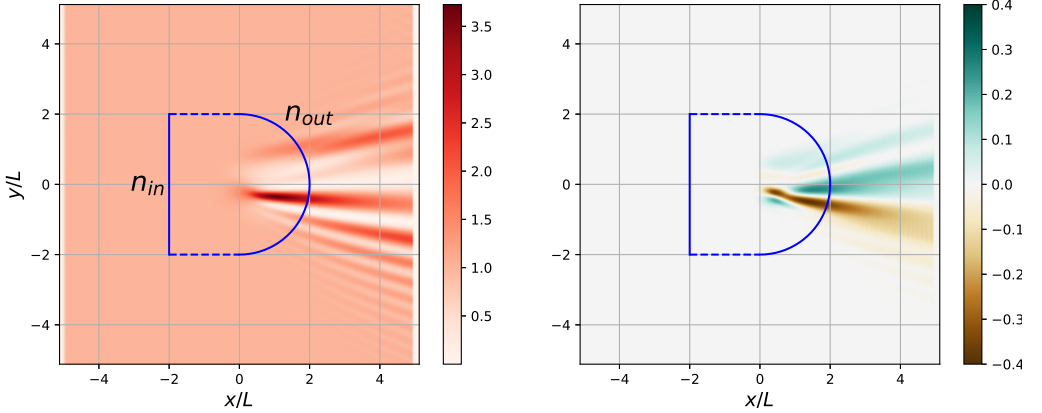
(a) Full wave field $\overline{\boldsymbol{\phi}}_w$.

(b) y component of $\overline{\boldsymbol{\phi}}_s$.

Figure 3: Phase-averaged wave flux for $(Ro_\zeta, Bu, K) = (0.60, 0.44, 4.3)$. The solid blue lines in the control volume are used to calculate the ratio S of the scattered wave flux to the incoming wave flux. The vector $\boldsymbol{n}_{in}$ ($\boldsymbol{n}_{out}$) is the unit vector associated with the incoming (outgoing) boundary.

energy is scattered between simulations, we define the scattering ratio as

$$S = \Phi_s/\Phi_{in}. \tag{2.11}$$

While this definition excludes the energy in the waves which have scattered back into the incoming direction due to the summation of wavevector rotations, the amount of energy in these waves is likely to be small compared to the total scattered energy. Note that since the vortex does not evolve in time, triad resonance theory implies that the scattered waves remain at the same frequency as in the incoming wave, and thus wave action and wave energy can be related by a constant (Kafiabad *et al.* 2019). We will calculate this quantity for all simulations in the next section, and use scaling laws to draw a relation from the non-dimensional variables to S.

232 **3. Results**

233   3.1. *Scattering Pattern*

234 The pattern of the wave flux density magnitude $|\overline{\boldsymbol{\phi}}_w|$, shown in figure 3a, consists of an
235 alternating 'constructive/destructive' interference pattern in the $x > 0$, $y < 0$ quadrant,
236 with the strongest flux values to be found near the exit of the vortex centre. In the $x > 0$,
237 $y > 0$ quadrant, there is a less well-defined scattering pattern. This qualitatively matches the
238 alternating flux pattern of Dunphy & Lamb (2014) for a barotropic vortex. We see that there
239 are regions on the outgoing side of the vortex where the flux has dropped to near-zero and
240 regions where the flux is more than three times that of the incoming wave.

241 To explain these features, we show the y-component of the scattered wave flux density, $\overline{\boldsymbol{\phi}}_s \cdot \hat{\boldsymbol{y}}$,
242 in figure 3b. Indeed, isolating the scattered part of the wave field eliminates the distracting
243 interference pattern with the unscattered wave. The y-component helps us distinguishing
244 three scattered beams. The first one, heareafter referred to as the central scattered beam
245 (CSB), crosses the centre of the vortex. In the cyclonic case presented in figure 3, this beam
246 is characterised by $\overline{\boldsymbol{\phi}}_s \cdot \hat{\boldsymbol{y}} < 0$. The other two beams emanate from the flanks of the vortex and
247 have $\overline{\boldsymbol{\phi}}_s \cdot \hat{\boldsymbol{y}} > 0$. We hereafter refer to these beams as right and left scattered beams (RSB and
248 LSB, respectively), in reference to whether they approach the left or right flank of the vortex
249 with respect to the direction of incident wave propagation.

250 We can now interpret that the region where we see a maximum in $|\overline{\boldsymbol{\phi}}_s|$ is where constructive
251 interference between the RSB and the CSB takes place. The regions where we find zero flux
252 are created by the RSB and CSB destructively interfering. In experiments with strong vortices,
253 we find lines of destructive interference due to a 180° phase difference between BSB and
254 CSB.

255 We claim that the scattering direction is mostly controlled by the vorticity. In our
256 simulations, the Coriolis parameter is negative, so the negative vorticity in the centre of the

cyclonic vortex produces the CSB, whose dominant wavevector rotates clockwise with respect to the incoming wavevector, and the opposite-sign vorticity region on the outside (recall figure 1a) produces the LSB and RSB, whose wavevector rotates anti-clockwise. Similarly, an anticylonic vortex produces a CSB whose dominant wavevector rotates anticlockwise, and produces the LSB and RSB whose wavevectors rotates clockwise. To support this claim, we now compare this pattern with the predictions from ray-tracing equations, which we recall in Appendix D, for an anticyclonic and cyclonic vortex of similar $|Ro_\zeta|$ and two different values of K.

Figure 4 shows that the rays which are initialised to only propagate through the positive/negative vorticity on the vortex edges are rotated anticlockwise/clockwise. The rays which travel through the centre are predominately rotated with the sign of the central vorticity. Thus ray tracing captures the "anticlockwise/clockwise/anticlockwise" scattered beam pattern for cyclonic vortices and the "clockwise/anticlockwise/clockwise" pattern for anticyclonic vortices. There are small differences in the ray tracing results when we compare cyclonic and anticyclonic vortices that are more than just a flip over the $y = 0$ axis for two reasons. First, anticyclonic vortices are "slimmer" (vorticity is more concentrated near the centre, over a shorter radius) compared to cyclonic vortices. Second, the refractive effects due to the height field in the term $d\omega/d\boldsymbol{x}$ in equation (D 1) differ between cyclonic and anticyclonic vortices. Indeed, an anticyclonic vortex centre rises above the mean depth, and since the group speed,

$$c_g = \frac{ghk}{(f^2 + ghk^2)^{1/2}}, \tag{3.1}$$

increases with depth, the waves travel faster through the centre of the vortex, and thus the height effects make the waves curve away from the centre line $y = 0$. Oppositely, cyclonic vortex centres dip below the mean depth, thus height effects make waves curve towards the

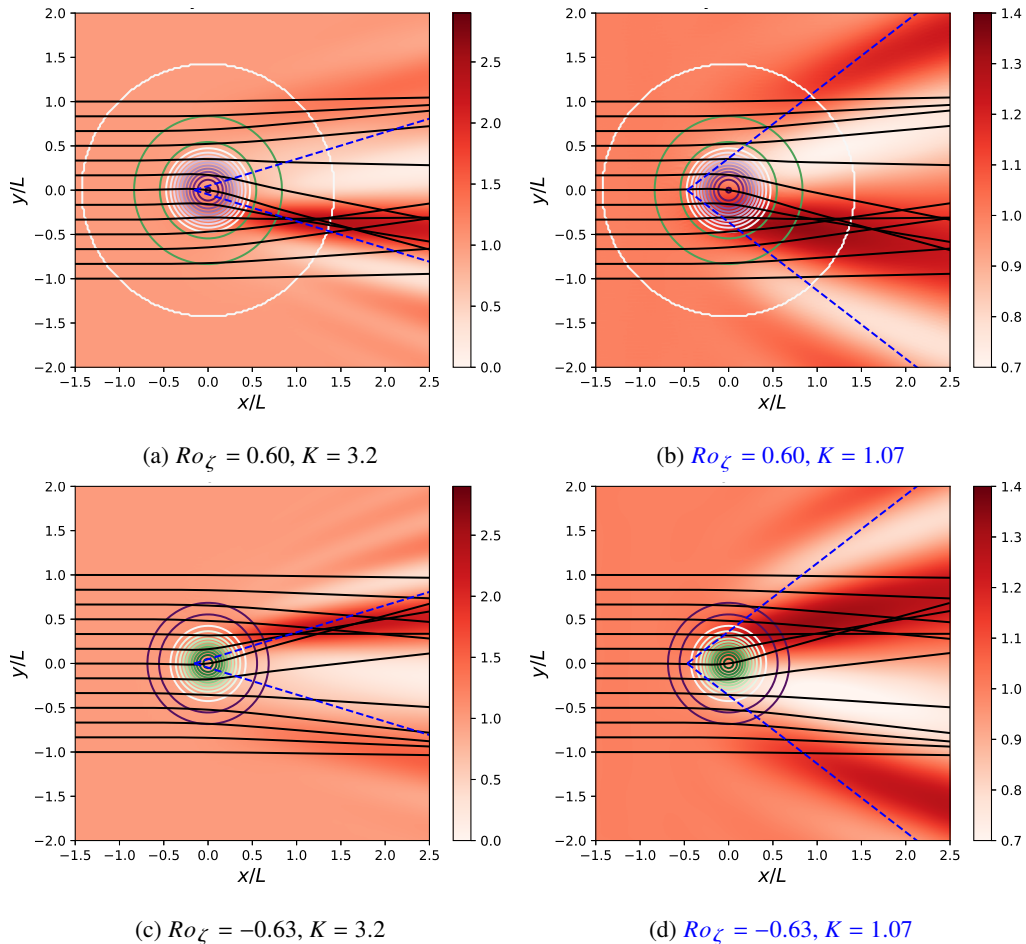(a) $Ro_\zeta = 0.60$, $K = 3.2$ (b) $Ro_\zeta = 0.60$, $K = 1.07$

(c) $Ro_\zeta = -0.63$, $K = 3.2$ (d) $Ro_\zeta = -0.63$, $K = 1.07$

Figure 4: Full flux field $\overline{\phi}_w$ for two similar but opposite-signed Ro_ζ and two wavelengths, see sub-captions. $Bu = 0.88$ in all cases. Ray-tracing lines are in black. The green and purple contours correspond to the colourbar shown in figure 1a. The two dashed blue lines represent the primary scattering angle predicted by triad resonance theory.

centre line. We checked that this effect is an order of magnitude smaller than the vorticity effect for balanced vortices.

The exact location where the rays converge aligns more closely with constructive interferences between CSB, LSB, and RSB, for $K = 3.2$ as opposed to $K = 1.07$. Note that the ray tracing predictions do not vary much for the range of K explored. Figure 4 reveals that the most striking limitation of ray tracing is that it does not capture the broad angles of

287 scattering, as can be seen from the interference pattern created by the incoming wave and
288 scattered waves.

289   The triad resonance theory formalism of Ward & Dewar (2010) can be used to predict the
290 principal scattering angle, θ_p, that is, the angle made between the incoming wave with wave
291 vector $\boldsymbol{k}_i$, and the scattered wave $\boldsymbol{k}_s$, which is determined by the main length scale in the
292 vortex $\boldsymbol{k}_v = 2\pi/L_a$. Assuming $|k_i| = |k_s|$ the principal angle can be calculated as a function
293 of K as

$$\theta_p = 2\arcsin((2K)^{-1}). \tag{3.2}$$

295 This implies that the angle of scattering would increase for smaller K. For $K = 1.07$, triad
296 resonance predicts that if there was only one balanced length scale L_a, the angle of scattering
297 would be $65°$, which is more than what we measure in our experiments as shown in figure 4.
298 We expect the discrepancy to be due to the multiple length scales and spatial variations of
299 the vorticity field experienced by the part of the plane wave passing through the centre. Thus,
300 even in this simple case, the principal scattering angle is not enough to describe this pattern.
301 Moreover, non-resonant, higher-order interactions would not be captured by triad resonance
302 theory. Thus, neither ray tracing nor triad resonances easily predict the exact nature of the
303 scattering pattern in this simple set-up.

304   *3.2. Scattering Statistics*

305 We now summarise the relationship between the scattered ratio S on the non-dimensional
306 numbers Bu, K, as well as one of the three vortex strength metrics Ro_b, Ro_ζ, ε. Visual
307 inspection reveals that for small values of the non-dimensional parameters, the scattering
308 ratio follows power law relations, while for large values, the scattering ratio approaches a
309 maximum of 100% conversion. The latter is similar to Dunphy & Lamb (2014), who carefully
310 checked that their Boussinesq eddies did not exchange net energy with the waves. Therefore,

	A	α	β	γ
Anticyclonic	10.67 ± 0.19	2.13 ± 0.01	-0.98 ± 0.01	2.10 ± 0.01
Cyclonic	5.35 ± 0.21	1.94 ± 0.01	-1.13 ± 0.01	2.10 ± 0.01
Combined	9.78 ± 0.59	2.10 ± 0.02	-0.99 ± 0.01	2.02 ± 0.02

Table 2: Optimisation parameters and their standard deviations for equation (3.3).

we propose to use an arctan relationship that is linear near the origin, and tends to a positive constant towards infinity. We considered several functions, none of which demonstrated superior performance as demonstrated in Appendix E, and settled on

$$S_Z^\theta = \frac{2}{\pi} \arctan(A Z^\alpha B u^\beta K^\gamma), \tag{3.3}$$

where the superscript θ denotes the optimised fit, $Z \in \{|Ro_b|, |Ro_\zeta|, \varepsilon\}$ is a placeholder for the three metrics of vorticity we will test, and where A, α, β and γ are the optimisation parameters. To find them, we fit the cyclonic experiments separately from the anticyclonic experiments, and in parallel, for comparison, we fit both datasets together, hereafter referred to as the "combined case". We use the least squares method to find the optimisation parameters using $Z = |Ro_b|$ which we show in table 2. We find that all the optimisation parameters have small errors, indicating that our fitting function is appropriate. The combined case is plotted in figure 5, where we have re-scaled the data based on the fit parameters. We see that anticyclonic vortices scatter energy at a slightly higher rate, as noted by the data points being slightly above the line of perfect fit, and as confirmed by table 2. However, the distinction is too small to conclusively claim that this is physical. Thus, we hereafter focus on the combined cases.

We now redo the optimisation using the enstrophy ε and the vorticity Rossby number Ro_ζ in addition to the bulk Rossby number Ro_b. The optimisation parameters for the three

	A	α	β	γ
Ro_b	9.78 ± 0.59	2.10 ± 0.02	-0.99 ± 0.01	2.02 ± 0.02
Ro_ζ	0.057 ± 0.001	1.77 ± 0.02	-1.02 ± 0.01	2.05 ± 0.02
ε	0.47 ± 0.02	1.03 ± 0.01	-0.98 ± 0.01	2.02 ± 0.02

Table 3: Optimisation parameters using three different vortex strength metrics in place of the bulk Rossby number in equation (3.3).

vortex strength metrics are shown in table 3. Figure 5 shows the three combined fits scaled by their respective parameters. They appear to be approximately equivalent; however, if we plot the same data on a logarithmic scale (figure 6), we observe that using the vorticity Rossby number Ro_ζ is not as effective as using enstrophy ε or bulk Rossby number Ro_b, which yield closer fits to data points. Both seem to result in round number scaling for α as well, with $\alpha \approx 2$ if $Z = Ro_b$, or $\alpha \approx 1$ if $Z = \varepsilon$. No matter which measure of vortex strength we use, we find that $\beta \approx -1$ and $\gamma \approx 2$. Simplifying the dependencies of S further, notice that

$$Ro_b/\sqrt{Bu} = U/\sqrt{gH} = U/c_0 = Fr, \qquad (3.4)$$

where the last number is the Froude number.

Collecting these approximations, we find that for small values of our non-dimensional parameters, equation (3.3) simplifies into

$$S \approx 5Fr^2 K^2, \qquad (3.5)$$

which we find to be reasonably accurate up to $S \approx 0.2$ (see figure 7). This simplified equation breaks down the scattering into a ratio of velocities multiplied by the ratio of length scales.
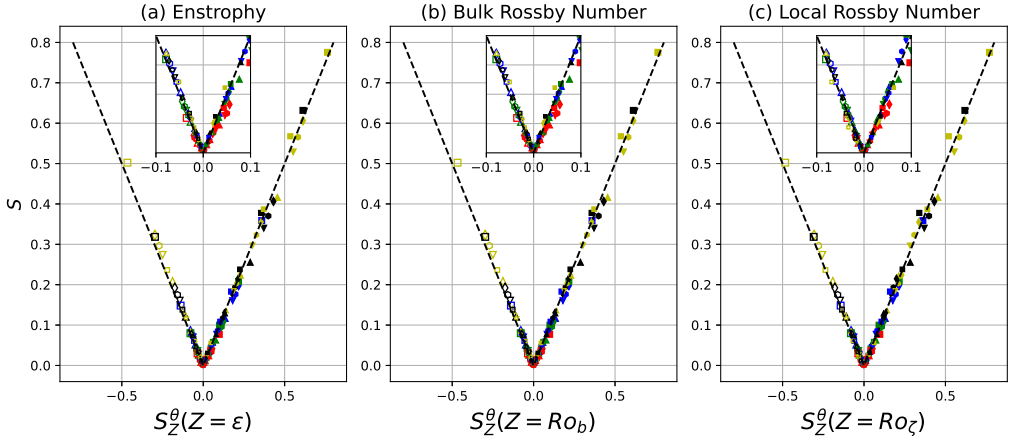
3.3. *Scaling Interpretation*

Figure 5: The *x*-axis shows the the data scaled by the fit function and respective optimisation parameters for the (a) enstrophy (b) bulk Rossby Number, (c) vorticity Rossby number. The size of the markers corresponds to the bulk Rossby number, the colours correspond to the adjusted ratio of length scales, and the markers correspond to unadjusted Burger number, as shown in the legend in figure 6. The black dashed lines are perfect fit lines.

Here we offer a possible interpretation for the seemingly round number scaling for Ro, K and Bu we find in the previous section. To interpret our results, we turn to Ward & Dewar (2010), who derived analytical solutions for a single wave mode interacting with a single length scale zero-frequency balanced mode by expressing the RSWEs in the form of interacting triads. In a simplified case, they show that the amplitude of the scattered wave mode A_s increases as a function of the balanced mode amplitude A_v, the incoming wave mode amplitude $A_{in}(t)$, and the interaction coefficient Γ, which is directly derived from the RSWEs. Specifically, this evolution is described by (adapted from Ward & Dewar 2010, eq. 3.11)

$$\frac{dA_s}{dt} = 2\Gamma A_v A_{in}. \tag{3.6}$$

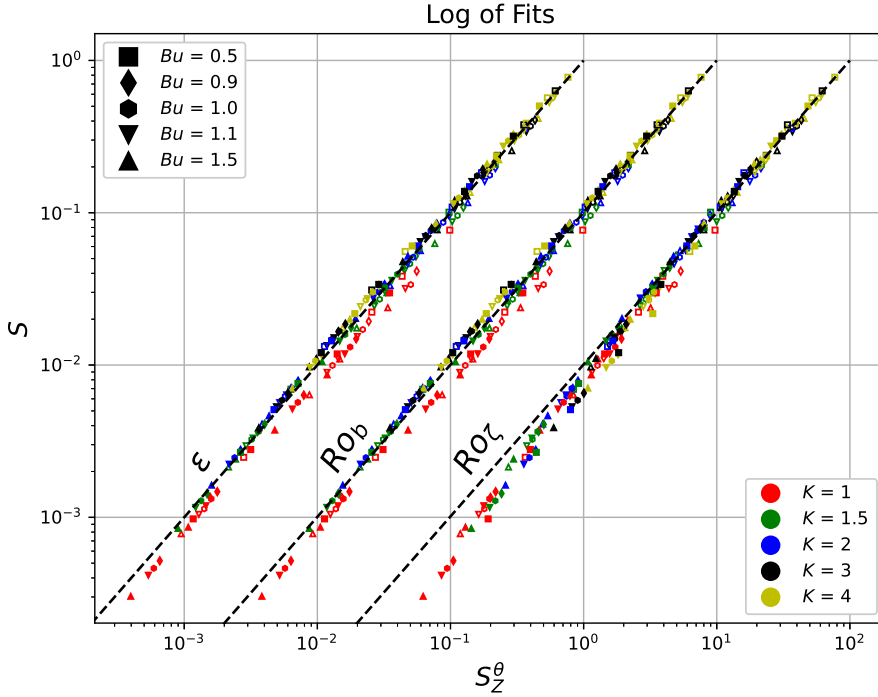Let's start by assuming that the wave mode amplitude is constant in time, which can be

Figure 6: The scattering ratio data in figure 5 shown in logarithmic scale. The black dashed lines show perfect fits.

356 achieved to a good approximation if the interaction is weak or brief. Then, we have

357
$$A_s/A_{in} = 2\Gamma A_v T_i \qquad (3.7)$$

358 where T_i is the time scale of the interaction. We can express this equation as a function of

359 our non dimensional variables. First, the amplitude of the vortex mode is proportional to the

360 bulk Rossby number $A_v \propto Ro_b$. Second, while the form of the interaction coefficient is very

361 complicated even for a single triad, Ward & Dewar (2010) find that for $K \gg \sqrt{Bu}$, $\Gamma \propto K$,

362 and that for $K \ll \sqrt{Bu}$, $\Gamma \propto K^2$. In our parameter regime, the Burger numbers are such

363 that $0.7 < \sqrt{Bu} = L_d/L < 1.6$, and we use waves with $0.5 \leqslant K \leqslant 4.5$. We are therefore

364 in an intermediate regime where the scaling Γ obeys cannot be estimated *a priori*. As we

365 are about to see, our simulations appear to be closer to a regime where $\Gamma \propto K$. Finally, the
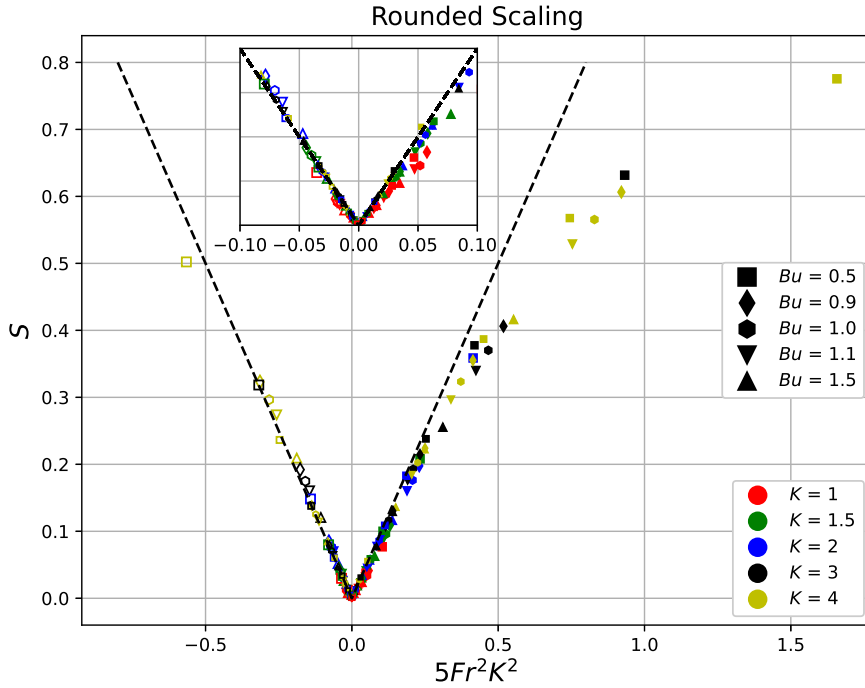
Figure 7: Simplified scaling for low scattering ratios as a function of only the Froude number $Fr = Ro_b/\sqrt{Bu}$ and length scales ratio K.

time scale of this interaction is proportional to the group speed. Note that f drops out of the scattering relation which is because the wave frequencies we examined are high enough compared to $|f|$, making the waves act more like non-rotating shallow water waves, and thus all group speeds are close to c_0. This time scale is then related to the Burger number with $T_i \propto 1/c_0 \propto Bu^{-0.5}$. Thus, assuming $\Gamma \propto K$, we have

$$S = \Phi_s/\Phi_{in} \sim (A_s/A_{in})^2 \propto Ro_b^2 K^2 Bu^{-1}, \qquad (3.8)$$

as we found using our theory-agnostic three-dimensional fits for small values of S.

As the time of interaction increases, the amplitude of the incoming wave decreases and hence the growth rate of the triads progressively decreases. This is an alternative interpretation

of the plateau that we see at high values of S, and why the arctan must be included in our scalings.

Recall that our approximately Gaussian vortex has multiple energetic length scales forming a spectrum of triads, each with their own value of Γ. Furthermore, each of the scattered waves that from due to the interaction of the incoming wave can than interact themselves with the vortex to create secondary triads. Thus, the fact that the specific vortex shape that we chose results in very similar scaling as the one length scale vortex in Ward & Dewar (2010) is remarkable. Furthermore, it may imply that similarly bell-shaped isolated vortices will have similar scalings. In light of these arguments, we expect that the details in the way they plateau to be different but similar isolated vortices likely follow the same growth rates for small values of S.

4. Discussion and Conclusion

We examined the scattering effect induced by an isolated vortex on a plane Poincaré wave. By removing the vortex and the incoming wave, we are able to visualise the scattered wave energy using the wave-averaged flux. The scattered energy forms in an "anticlockwise/clockwise/anticlockwise" ("clockwise, anticlockwise, clockwise") pattern, which we attribute to the strong negative (positive) vorticity in the interior for (anti)cyclones, and weaker positive (negative) vorticity in the exterior. The ray-tracing equations capture this alternating pattern, but the locations of ray convergence do not always align with the locations of maximum amplitude in the simulation data. We see the expected limitations of ray tracing when the vortex and wavelength are of comparable size, most strikingly when $K = 1$ where the angle of scattering it predicts is much shallower than those we see in the simulations. The scattering pattern of anticyclonic and cyclonic vortices of similar Rossby number magnitude lead to slightly different patterns due to the difference in shape after cyclogeostrophic balance, but the effect is minor in our parameter regime.

400   Overall, our scattering patterns qualitatively agree with those of the Boussinesq simulations

401   of Dunphy & Lamb (2014, figure 5) for barotropic vortices, which gives us confidence that

402   RSWEs are a appropriate model to study internal tide/vortex interactions. Note that these

403   authors mention that their attempts at interpreting the scattering pattern with ray tracing had

404   failed, leading them to conclude that this approach is not appropriate in their regime. Here,

405   we interpret these "hot-cold" patterns as interference patterns between three scattered beams

406   and the transmitted incident wave, whose general features and directions qualitatively agree

407   with ray tracing predictions. As such, our interpretation rehabilitates ray tracing to some

408   degree. However, it fails to predict the very existence of a transmitted plane wave, nor can

409   it predict how wide the scattering pattern is, even in experiments with high K's. Therefore,

410   previous work based on ray tracing (e.g., Rainville & Pinkel 2006; Chavanne *et al.* 2010)

411   should be interpreted with caution.

412   On a related subject, figure 8 of the aforecited article shows very different scattering

413   patterns for baroclinic vortices. Interactions between baroclinic modes could yield different

414   results, which could be investigated with multi-layer RSWEs in future studies.

415   Using three-dimensional fits, we derived a relation that gives the scattering ratio as a

416   function of the Burger number Bu, the ratio of the vortex to the wave length scale K, and

417   a measure of the vortex strength, which we quantify through the bulk Rossby number Ro_b,

418   the vorticity Rossby number Ro_ζ, and the enstrophy ε. We observe that the fit is successful

419   when an arctan is used with a power law combination of the three non-dimensional numbers

420   as the argument. We find that the bulk Rossby number Ro_b and the enstrophy ε are the most

421   suitable vortex strength metrics to predict the scattering ratio, while the vorticity Rossby

422   number Ro_ζ yields a less suitable approximation. We find round number scalings for the

423   argument in the arctan, specifically, $\tan(\pi S/2) \propto Ro_b^2 K^2 Bu^{-1}$. This aligns with the triad

424   formalism from Ward & Dewar (2010), where the growth rate of a single triad wave is shown

to be proportional to the amplitude of the vortex, which is determined by Ro_b, the time of interaction, which is determined by Bu, and the triad interaction coefficient which is related to K. Since our theory-agnostic fits using a Gaussian vortex result in the same scaling as the single-mode example in Ward & Dewar (2010), it may imply that these scalings would be similar for a variety of isolated vortices with bell-shaped height fields, at least for small values of S. For small scattering ratios, these dependencies reduce to $S \propto Fr^2 K^2$.

Independently, Ito & Nakamura (2023) non-dimensionalise the equations of motions first and show that $FrK^{-1} = \frac{U}{c_0}\frac{\lambda}{L}$ can be used to separate the vortical effects on the wave from the linear equations. They vary this parameter as a whole to show different scattering regimes and patterns. At higher values, they show that the wave can become trapped in the vortex. While their scaling significantly differs from ours, note that we obtained our results by measuring the scattered energy in a theory-agnostic fashion. Furthermore, our scalings are consistent with the theory of Ward & Dewar (2010), who find that stronger triads form at large values of K. Additionally, Coste *et al.* (1999), who investigate how a vertical vortex in solid-body rotation creates phase dislocations on an incoming wave, found a similar ratio to FrK.

Although we did not vary Fr_w, we do not anticipate the results to vary until the wave has enough energy to alter the structure of the vortex itself (e.g., via wave capture; Bühler & McIntyre 2005), or to undergo destabilising non-linear processes. To study the non-linear wave regime is likely to represent an avenue for further research.

Most eddies with characteristic width L are well approximated by a Gaussian profile within the radius $L/3$ from their centre (Chelton et al., 2011) which makes our scaling relation broadly applicable. To find a more general scaling relation, we could extend our analysis to other vortex profiles, and in the process check how robust our scaling relations are to the vortex shape. For example, we could start with stable oblate vortices, which would

add another degree of freedom to our scaling relations, and produce asymmetries in the scattering pattern depending on the incoming wave direction.

The parameter range we explored covers a broad range of physical regimes in which an IT will interact with eddies in the ocean. We did not explore waves larger than the vortices, but we can extrapolate from our data that $K < 1$ would lead to little scattering ($S < 0.1$) even at vorticity Rossby numbers of $O(1)$ and Burger numbers of $O(0.1)$. We also did not explore simulations with $|Ro_\zeta| \gg 1$ and $Bu < 0.4$, but since we came close to complete scattering with $K = 4$, we can extrapolate to find which simulations would lead to completely scattered waves ($S = 1$). For example, if we had Rossby and Burger numbers equal to one, a wave with $K = 5$ would already lead to almost complete scattering with $S = 0.97$. In open ocean regimes, mesoscale eddies are about the size of mode-1 M_2 tides ($K = 1$) and have $Ro_b = 0.01$ and $Bu \approx 1$, so we predict that the scattering will be small at $S < 1\%$. In submesoscale regimes, near coasts and strong currents, where mode 5 ITs interact with vortices of $Ro_b > 0.1$, the scattering ratio will be $> 10\%$. These results inspire useful diagnostics for satellite altimetry data and global circulation models to determine where errors may be at their highest given the local vorticity field, IT mode, local rotation rate, and stratification. Future work on our idealised model should include simple time-varying balanced flows (e.g., vortex pairs), oblate vortices, and adding vertical layers to include the effects of baroclinicity in the balanced flow.

Author ORCIDs. J.U.: 0009-0007-8831-8898; N.G.: 0000-0003-4045-2143.

Appendix A. Cyclogeostrophic Balance Iterative Method

To create a time-independent balanced vortex with a non-zero Rossby number we need to include the effects of advection. Thus, the vortex must satisfy ,

$$\boldsymbol{u} \cdot \nabla \boldsymbol{u} + f\hat{z} \times \boldsymbol{u} = -g\nabla\eta. \tag{A 1}$$

Equation A 1 can be solved analytically for some axis-symmetric cases; however, we can extend this to larger Ro if we use the iterative method in Penven *et al.* (2014), which we describe below.

Let the velocity $\boldsymbol{u_g}$ associated with the geostrophic flow be $f\hat{z} \times \boldsymbol{u_g} = -g\nabla\eta$. We rearrange equation A 1 to give

$$\boldsymbol{u} - \hat{z}f^{-1} \times (\boldsymbol{u} \cdot \nabla \boldsymbol{u}) = \boldsymbol{u_g}. \tag{A 2}$$

It is then possible to approximate the solution by iterating equation A 2 as follows,

$$\boldsymbol{u}^{(n+1)} = \boldsymbol{u_g} + \hat{z}f^{-1} \times (\boldsymbol{u}^{(n)} \cdot \nabla \boldsymbol{u}^{(n)}) \tag{A 3}$$

while max $|\boldsymbol{u}^{(n+1)} - \boldsymbol{u}^{(n)}| < 10^{-4} ms^{-1}$ or until $\boldsymbol{u}^{(n+1)} > \boldsymbol{u}^{(n)}$. These adjusted velocities are used to initialise the velocity field in the vortex simulation.

Appendix B. Sponge layers

The Tukey window is used to force and absorb waves on either side of the domain. It has the profile of a tapered cosine at the edges and a constant at the center. This is useful to ensure that the waves achieve the amplitude they are prescribed.

494 The formula for the Tukey window is shown below,

$$\Pi(x, x_0) = \begin{cases} 0 & x < x_0 \\[2mm] \frac{1}{2}\left\{1 - \cos\left[\frac{2\pi x}{\Delta\lambda}\right]\right\} & x_0 \leqslant x < \Delta\lambda/2 + x_0 \\[2mm] 1 & \Delta\lambda/2 + x_0 \leqslant x < \lambda - \Delta\lambda/2 + x_0, \\[2mm] \frac{1}{2}\left\{1 - \cos\left[\frac{2\pi x}{\Delta\lambda} - \frac{2\pi}{\Delta}\right]\right\} & \lambda - \Delta\lambda/2 + x_0 \leqslant x < \lambda + x_0, \\[2mm] 0 & \lambda + x_0 \leqslant x, \end{cases} \quad \text{(B 1)}$$

496 where $\Delta = 0.7$.

497 The vortex adjustment simulation requires a sponge layer to absorb the waves that radiate

498 during the adjustment process. To absorb waves with minimal reflection, a circular sponge

499 layer is set at a distance $R_1 = 2L$, which increases linearly until $R_2 = 2.8L$ as shown below.

$$CS(r) = \begin{cases} 0 & r \leqslant R_1, \\[2mm] (r - R_1)/(R_2 - R_1) & R_1 \leqslant r \leqslant R_2, \\[2mm] 1 & R_2 \leqslant r. \end{cases} \quad \text{(B 2)}$$

501 For simulations with high Rossby numbers, there does tend to be some reflection, but has

502 a small effect on the diagnostics.

503 **Appendix C. Linear Shallow Water Equations**

504 The linear shallow-water equations are as follows,

$$\partial_t \boldsymbol{u} + f\hat{z} \times \boldsymbol{u} = -g\nabla\eta \qquad \text{and} \qquad \partial_t h + H\nabla \cdot (\boldsymbol{u}) = 0, \qquad \text{(C 1)}$$

506 where f is constant in this article. Let us assume a wave solution that is only propagating in

507 one direction, so that $V = [\tilde{u}, \tilde{v}, \tilde{h}]e^{ikx}$ we can then rewrite equations C 1 as

508
$$\partial_t V + MV = 0, \qquad \text{where} \qquad M = \begin{bmatrix} 0 & -f & ikg \\ f & 0 & 0 \\ ikH & 0 & 0 \end{bmatrix}. \tag{C 2}$$

509 The three eigenvalues of M are proportional to the frequencies of the wave modes. They are

510 $\omega_G = 0$ and $\omega_W^{(\pm)} = \pm\sqrt{f^2 + gHk^2}$, with corresponding eigenvectors

511
$$G = \left[0, \ 1, \ -\frac{if}{gk}\right] \qquad \text{and} \qquad W_\pm = \left[\frac{\omega_W^{(\pm)}}{f}, \ 1, \ \frac{-ikH}{f}\right]. \tag{C 3}$$

512 The eigenvectors $W_\pm$ are used to force the wave from the right.

513 **Appendix D. Ray Tracing**

514 Ray tracing is a method to track the position and wavevector of a wavepacket through a fluid

515 media, assuming that the wavelength is small compared to the length scales in the media.

516 Let the position of the wavepacket be x with wavevector k, and it made to pass through a

517 velocity field $U = (U, V)$, then the ray tracing equations read,

518
$$dx/dt = U + d\omega/dk \qquad \text{and} \qquad dk/dt = -(\nabla U) \cdot k - d\omega/dx, \tag{D 1}$$

519 where $\omega = \sqrt{f^2 + ghk^2}$. The first equation describes the evolution of the wave packet position

520 due to the advection of the media and the group speed. The second equation describes the

521 refraction of the wave vector as a result of strain and shear and due to the change in frequency.

	A	α	β	γ
Sigmoid	8.18 ± 0.02	1.86 ± 0.02	-0.85 ± 0.02	1.80 ± 0.02
Tanh	4.08 ± 0.03	1.86 ± 0.03	-0.85 ± 0.01	1.80 ± 0.02

Table 4: Optimisation parameters for alternative fitting functions using $Z = Ro_b$.
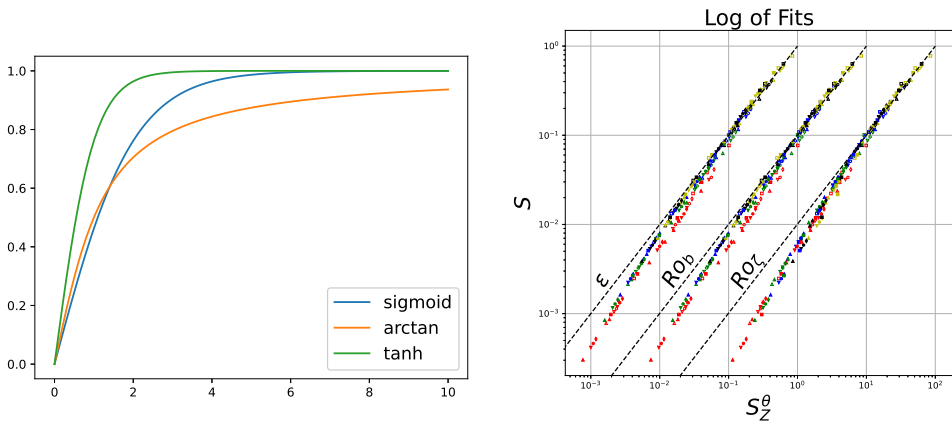
(a) Fitting curves.

(b) Sigmoid fit using the same legend from figure 6.

Figure 8

Appendix E. Alternative Fitting Functions

Here we explore two other choices for fitting function which are linear for small values of S and then plateau towards one, namely a sigmoid and a tanh defined below,

$$\check{S}_Z^\theta = 2(1 + \exp[-AZ^\alpha Bu^\beta K^\gamma]), \tag{E 1}$$

$$\check{S}_Z^\theta = \tanh[AZ^\alpha Bu^\beta K^\gamma]. \tag{E 2}$$

The curves for these functions are shown in figure 8a and the fit parameters are shown in table 4. We find that the fit parameters for both the sigmoid and the tanh can no longer be rounded to whole numbers as we were able to do using arctan. Furthermore, the fit has become worse for both these functions, as shown in figure 8b for the sigmoid (to compare

with figure 6), because both functions plateau too quickly resulting in inaccurate fitting for low values of S. While the arctan we use in the main text models the data well for all values of S, we don't believe this implies that there is something physical about arctan, but rather that it is likely just a convenient choice to model the plateau.

REFERENCES

BARTELLO, P. 1995 Geostrophic adjustment and inverse cascades in rotating stratified turbulence. *Journal of the Atmospheric Sciences* **52** (24), 4410–4428.

BÜHLER, OLIVER 2014 *Waves and Mean Flows*. Cambridge University Press.

BÜHLER, OLIVER & MCINTYRE, MICHAEL E. 2005 Wave capture and wave-vortex duality. *Journal of Fluid Mechanics* **534**, 67–95.

BURNS, KEATON J., VASIL, GEOFFREY M., OISHI, JEFFREY S., LECOANET, DANIEL & BROWN, BENJAMIN P. 2020 Dedalus: A flexible framework for numerical simulations with spectral methods. *Physical Review Research* **2** (2), 023068.

CHAVANNE, C., FLAMENT, P., LUTHER, D. & GURGEL, K-W. 2010 The Surface Expression of Semidiurnal Internal Tides near a Strong Source at Hawaii. Part II: Interactions with Mesoscale Currents*. *Journal of Physical Oceanography* **40** (6), 1180–1200.

COSTE, CHRISTOPHE, LUND, FERNANDO & UMEKI, MAKOTO 1999 Scattering of dislocated wave fronts by vertical vorticity and the Aharonov-Bohm effect. I. Shallow water. *Physical Review E* **60** (4), 4908–4916.

DUNPHY, MICHAEL & LAMB, KEVIN G. 2014 Focusing and vertical mode scattering of the first mode internal tide by mesoscale eddy interaction. *Journal of Geophysical Research: Oceans* **119** (1), 523–536.

EGBERT, G. D. & RAY, R. D. 2000 Significant dissipation of tidal energy in the deep ocean inferred from satellite altimeter data. *Nature* **405** (6788), 775–778.

EGBERT, GARY D. & RAY, RICHARD D. 2003 Semi-diurnal and diurnal tidal dissipation from TOPEX/Poseidon altimetry. *Geophysical Research Letters* **30** (17), n/a–n/a.

FU, LEE-LUENG, CHRISTENSEN, EDWARD J., YAMARONE, CHARLES A., LEFEBVRE, MICHEL, MÉNARD, YVES, DORRER, MICHEL & ESCUDIER, PHILIPPE 1994 TOPEX/POSEIDON mission overview. *Journal of Geophysical Research: Oceans* **99** (C12), 24369–24381.

558 GARRETT, CHRIS & KUNZE, ERIC 2007 Internal Tide Generation in the Deep Ocean. *Annual Review of Fluid*
559   *Mechanics* **39** (1), 57–87.

560 ITO, KAORU & NAKAMURA, TOMOHIRO 2023 Three Regimes of Internal Gravity Wave–Stable Vortex
561   Interaction Classified by a Nondimensional Parameter δ: Scattering, Wheel-Trapping, and Spiral-
562   Trapping with Vortex Deformation. *Journal of Physical Oceanography* **53** (4), 1087–1106.

563 KAFIABAD, HOSSEIN A., SAVVA, MILES A. C. & VANNESTE, JACQUES 2019 Diffusion of inertia-gravity waves
564   by geostrophic turbulence. *Journal of Fluid Mechanics* **869**, R7.

565 DE LAVERGNE, C., FALAHAT, S., MADEC, G., ROQUET, F., NYCANDER, J. & VIC, C. 2019 Toward global maps
566   of internal tide energy sinks. *Ocean Modelling* **137**, 52–75.

567 LELONG, M. PASCALE & RILEY, JAMES J. 1991 Internal wave—vortical mode interactions in strongly stratified
568   flows. *Journal of Fluid Mechanics* **232** (-1), 1.

569 MCWILLIAMS, JAMES C. 2016 Submesoscale currents in the ocean. *Proceedings of the Royal Society A:*
570   *Mathematical, Physical and Engineering Sciences* **472** (2189), 20160117.

571 MORROW, ROSEMARY, FU, LEE-LUENG, ARDHUIN, FABRICE, BENKIRAN, MOUNIR, CHAPRON, BERTRAND,
572   COSME, EMMANUEL, D'OVIDIO, FRANCESCO, FARRAR, J. THOMAS, GILLE, SARAH T., LAPEYRE,
573   GUILLAUME, LE TRAON, PIERRE-YVES, PASCUAL, ANANDA, PONTE, AURÉLIEN, QIU, BO, RASCLE,
574   NICOLAS, UBELMANN, CLEMENT, WANG, JINBO & ZARON, EDWARD D. 2019 Global Observations
575   of Fine-Scale Ocean Surface Topography With the Surface Water and Ocean Topography (SWOT)
576   Mission. *Frontiers in Marine Science* **6**.

577 NASH, JONATHAN, SHROYER, EMILY, KELLY, SAMUEL, INALL, MARK, DUDA, TIMOTHY, LEVINE, MURRAY,
578   JONES, NICOLE & MUSGRAVE, RUTH 2012 Are Any Coastal Internal Tides Predictable? *Oceanography*
579   **25** (2), 80–95.

580 PENVEN, PIERRICK, HALO, ISSUFO, POUS, STÉPHANE & MARIÉ, LOUIS 2014 Cyclogeostrophic balance in the
581   Mozambique Channel. *Journal of Geophysical Research: Oceans* **119** (2), 1054–1067.

582 RAINVILLE, LUC & PINKEL, ROBERT 2006 Propagation of Low-Mode Internal Waves through the Ocean.
583   *Journal of Physical Oceanography* **36** (6), 1220–1236.

584 SAVVA, M.A.C., KAFIABAD, H.A. & VANNESTE, JACQUES 2021 Inertia-gravity-wave scattering by three-
585   dimensional geostrophic turbulence. *Journal of Fluid Mechanics* **916**, A6, arXiv: 2008.02203.

586 SAVVA, MILES A. C. & VANNESTE, JACQUES 2018 Scattering of internal tides by barotropic quasigeostrophic
587   flows. *Journal of Fluid Mechanics* **856**, 504–530.

588 SHAKESPEARE, CALLUM J. 2016 Curved Density Fronts: Cyclogeostrophic Adjustment and Frontogenesis.
589   *Journal of Physical Oceanography* **46** (10), 3193–3207.

590 VALLIS, GEOFFREY K. 2017 *Atmospheric and Oceanic Fluid Dynamics*, 2nd edn. Cambridge University
591   Press.

592 WARD, MARSHALL L. & DEWAR, WILLIAM K. 2010 Scattering of gravity waves by potential vorticity in a
593   shallow-water fluid. *Journal of Fluid Mechanics* **663**, 478–506.

594 ZHAO, ZHONGXIANG, ALFORD, MATTHEW H., GIRTON, JAMES B., RAINVILLE, LUC & SIMMONS, HARPER L.
595   2016 Global Observations of Open-Ocean Mode-1 M2 Internal Tides. *Journal of Physical
596   Oceanography* **46** (6), 1657–1684.